Mine Water and the Environment (2021) 40:398–414
https://doi.org/10.1007/s10230-021-00772-4

TECHNICAL ARTICLE

Micro-fracture Precursors of Water Flow Channels Induced by Coal Mining: A Case Study

Guanwen Cheng[1,2] · Chunan Tang[3] · Lianchong Li[1] · Xiaoyu Chuai[4] · Tianhong Yang[1] · Like Wei[5]

Received: 10 October 2019 / Accepted: 13 March 2021 / Published online: 5 May 2021

Abstract

The evolution of water flow channels typically includes a micro-fracture precursor, especially during deep mining. However, this precursor has not been well characterized. To get more insight into this precursor and its development, the no. 22517 panel in the Dongjiahe coal mine was studied using microseismic monitoring. The energy density of microseismic events was used to identify the spatial location and formation process of the water flow channels. Microseismic focal parameters, such as seismic energy, seismic potency, apparent stress, seismic moment, apparent volume, energy index, and the Gutenberg-Richter b value were determined for the micro-fracture precursors of the water flow channels. The cumulative apparent volume increased significantly and the Gutenberg-Richter b value decreased rapidly, corresponding to the micro-fracture precursor of the water flow channel. Based on the results, a Gutenberg-Richter b value of 0.7 may be an early warning threshold for the formation of a water-flow channel. Finally, a real-time early warning method for water inrush disasters in floor was established based on microseismic monitoring, geophysics, and the water inrush coefficient.

Keywords Micro-fracture monitoring · Precursor · Ordovician limestone water · Gutenberg-Richter b value · Water inrush coefficient

Introduction

Coal remains an irreplaceable energy for the next few decades in China, where the coal is mainly stored in Permo-Carboniferous strata. Ordovician limestone, which is usually situated below the Permo-Carboniferous strata, is a strong regional aquifer in north China, where nearly 60% of China's coal reserves are located. Mines in this area are highly prone to major floor water inrush disasters. Floor-confined water threatens nearly 50% of China's major coal mines, with reserves of 2.5×10^{13} kg. The probability of water inrush disasters increases sharply with high water pressure and ground pressure, which have accompanied eastern China's increased mining depths.

Many scholars have carried out studies attempting to predict water inrush disasters induced by mining, using theoretical calculations, mathematical models, and on-site monitoring. As an example of a theoretical calculation, Siliesaliefu assumed the floor strata in a panel to be a beam under uniform load, while the mechanical problem of floor failure induced by underground mining was simplified as a simply supported beam under uniformly distributed loads (Zhang 2016). Xu et al. (2017) derived a semi-analytical solution to determine the minimum safety thickness of rock to resist water inrush disasters from filling-type karst caves. Li et al. (2019) deduced a way to calculate the critical condition of failure of an aquiclude under the presence of a fault using brittle fracture criteria and the shear failure limit equilibrium condition.

✉ Lianchong Li
lilianchong@mail.neu.edu.cn

1 Center for Rock Instability and Seismicity Research, Northeastern University, Shenyang 110819, China

2 Laboratory of Seismology and Physics of Earth's Interior, School of Earth and Space Sciences, University of Science and Technology of China, Hefei 230026, China

3 State Key Laboratory of Coastal and Offshore Engineering, Dalian University of Technology, Dalian 116023, China

4 He Bei Coal Research Institute, Xingtai 05400, China

5 Ministry of Emergency Management Information Institute, Beijing 10029, China

An empirical formula was proposed to calculate the water inrush coefficient, and this formula has been widely used in China (Zhang 2016). Based on this formula, a coefficient-unit inflow method of water inrush disasters was proposed by Qiao et al. (2009). Meng et al. (2012) improved the formula to calculate the water inrush coefficient by considering the height of the zone of water rising from the confined aquifer and the floor failure depth. Fan et al. (2019) adopted the water inrush coefficient to evaluate the risk of water inrush disasters in separate layers. These theoretical methods provide insight into the mechanism of water inrush disaster induced by mining activity in coal mines. However, due to the complexity of geological conditions and in situ stress conditions, there was inherent inaccuracy of their predictive abilities.

In recent years, many scholars have used mathematical models to predict water inrush disasters based on the hydrogeological conditions. These mathematical models included catastrophe theory (Hua et al. 2011), variable-weight model and unascertained measure theory (Wu et al. 2017), fuzzy mathematics (Yang et al. 2017), Bayesian networks (Wu et al. 2016), attribute mathematical theory (Li et al. 2015), intelligent machine-learning algorithm (Zhao al. 2018), and analytic hierarchy process (Du et al. 2017; Wu et al. 2015). However, these models lacked physical meaning, and the validity of predictions of water inrush disasters using these models was uncertain due to the complexity of hydrological conditions in the field, making it very difficult to use mathematical models to accurately predict inrush disasters before mining. Thus, in-site monitoring is key for more accurate predictions.

The evolution of water flow channels typically begins with a micro-fracture precursor, especially under the high-pressure conditions of deep mining. Microseismic (MS) monitoring is an important tool to monitor micro-fracture precursors. According to Liu et al. (2014) and Zhang et al. (2016), a combination of MS monitoring and numerical analysis of damaged zones can help reveal the formation process of the flow channel. Zhou et al. (2017) analyzed the spatial and temporal behaviors of density distribution, focal parameters, and cracking-type MS events and correlated them with the formation processes of a local flow channel. However, the micro-fracture precursor of water-flow channels was not clearly revealed, limiting the ability to predict an inrush disaster.

In general, there are two types of fractures that may constitute water flow channels. The first is a crack caused by the failure of rock under the action of mining stress and seepage pressure. The second is a crack formed by the activation and further failure of geological structures in the rock mass due to the mining stress and seepage pressure. Accurate monitoring of the spatial distribution and evolution process of these two kinds of fractures is the key to determining the spatial location of the water flow channels and predicting them.

In view of these two failure modes, many scholars have carried out studies at the laboratory scale by AE monitoring. Lei et al. (2003) carried out triaxial compression experiments with joints, and stated that the spatial distribution and formation process of cracks induced by the activation of primary joints were closely related to the spatial aggregation and evolution of AE events. Chen et al. (2012) carried out conventional triaxial compression experiments, Li et al. (2013) conducted direct tensile tests, and Xie et al. (2011) conducted Brazilian splitting tests. Their research results showed that the spatial distribution and formation process of shear and tensile cracks in rock specimens were consistent with the spatial aggregation and evolution of AE events. This indicated that it was feasible to use MS monitoring technology to monitor the formation of water flow channels.

This focus of this study was the no. 22517 panel in the Dongjiahe coal mine. An MS monitoring system was established to study the micro-fracture precursors and the focal parameters for the micro-fracture precursor were determined. A MS monitoring system was installed to monitor floor MS events during mining activities in the no. 22517 panel. Next, the formation process of water-flow channels was identified in the panel by analyzing changes in hydrological and geological conditions, water quality, and water inflow during the mining process, along with the MS monitoring results. Finally, the way these parameters varied were studied.

Methodology

Relationship Between MS Events and Water Flow Channels

To form water flow channels, the micro-fracture events must meet two conditions. First, the micro-fractures must be near each other and second, the scale of the micro-fracture events has to be large enough to make the micro-fractures connect. Seismic energy is an important parameter for measuring the scale of micro-fracture events. If the seismic energy of each MS event is very large, only a few MS events are needed to connect the micro-fractures. If the seismic energy of each MS event is very small, a large number of MS events are needed to ensure a micro-fracture connection. Thus, we used the energy density of MS events to comprehensively determine the energy aggregation and quantity aggregation of MS events. The

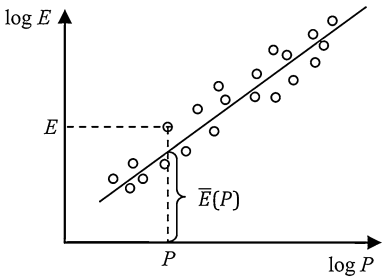

Fig. 1 Linear relationship between the logarithm of seismic potency and the logarithm of seismic energy (Xiao et al. 2016)

energy density of MS events was defined as the sum of all MS events in unit volume. The threshold of the energy density of MS events is related to the panel depth, lithology, and structural stress. Taking the no. 22517 panel in the Dongjiahe coal mine as an example, the threshold of the energy density of MS events was determined through the mutual verification of the various monitoring results, so as to provide reference for mines with similar engineering geological conditions.

Potential Precursory Indicators of Water Flow Channels

MS sensors can be used to monitor the real-time waveforms of elastic wave motion caused by the micro-fracturing of a rock mass. Using the waveforms received by different sensors, the arrival times of P or S waves can be determined. Based on the P wave and S wave velocity, the position and time of the MS events can then be calculated by the three-ball intersection principle. Finally, the focal parameters of moment magnitude, seismic moment,

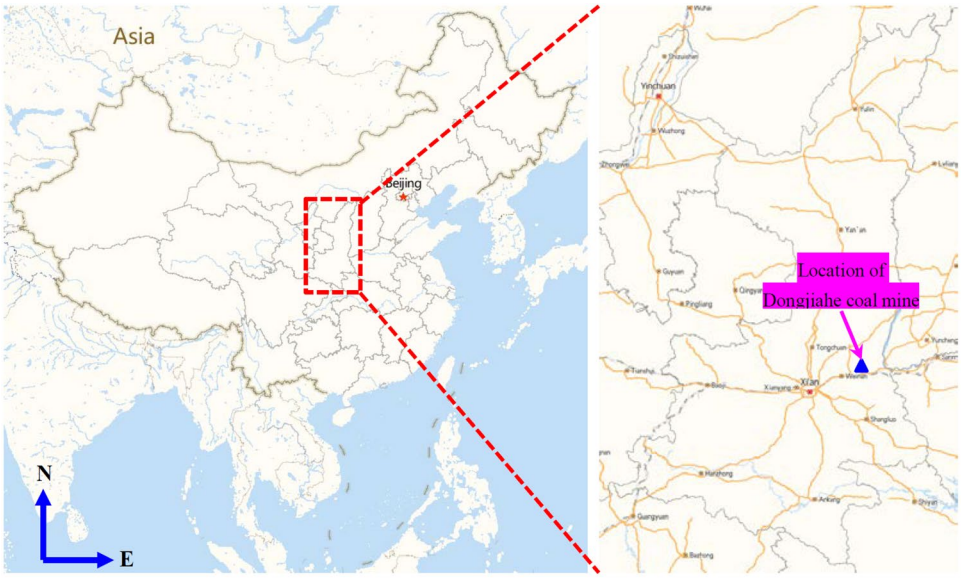

(a) Location of Dongjiahe coal mine

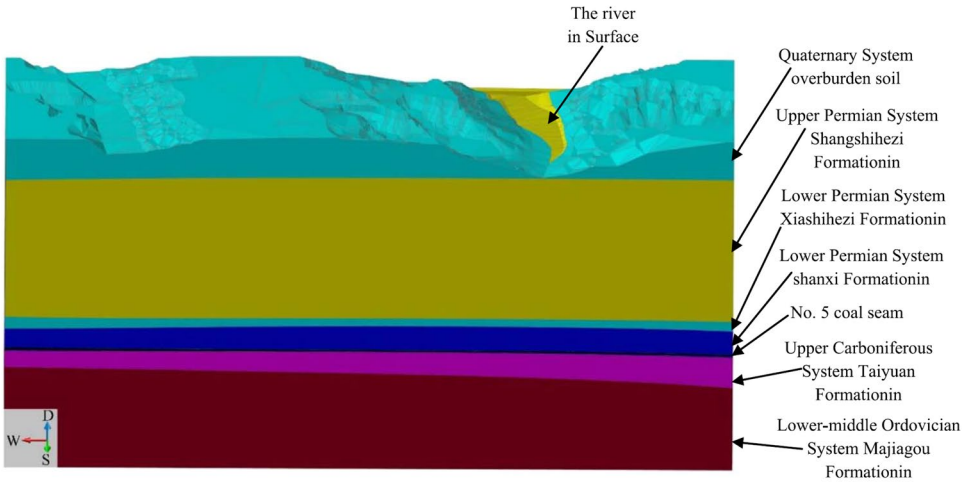

(b) 3D map of the No. 22517 Panel (***Cheng et al., 2017***)

Fig. 2 General geological situation of the no. 22517 panel in the Dongjiahe coal mine

seismic energy, ratio of S-wave to P-wave energy, source radius, asperity radius, static stress drop, apparent stress, dynamic stress drop, maximum displacement, peak velocity parameter, and peak acceleration parameter are calculated using methods of quantitative seismology based on the waves received by different sensors, the location of MS events, and the attenuation of wave propagation in the rock mass.

Lynch et al. (2004) and Mendecki et al. (2010) used seismic energy, seismic potency, apparent stress, cumulative apparent volume, energy index, and other parameters to predict large MS events. Liu et al. (2013) used seismic moment, Gutenberg-Richter b value, spatial correlation length, and fractal characteristics to study the damage evolution characteristics of surrounding rocks during mining activities to obtain precursory information of rock-burst disasters in the Hongtoushan Copper Mine. Chen et al. (2011), Xiao et al. (2016), and Yu et al. (2015) applied apparent volume, apparent stress, energy index, and Gutenberg-Richter b value to study early warning of rock-burst disasters in a deep tunnel of the Jinping II Hydropower Station. Cheng et al. (2019) used the Gutenberg-Richter b value to study the mining-induced brittle fault activation process. Since these and other previous studies have shown that seismic energy,

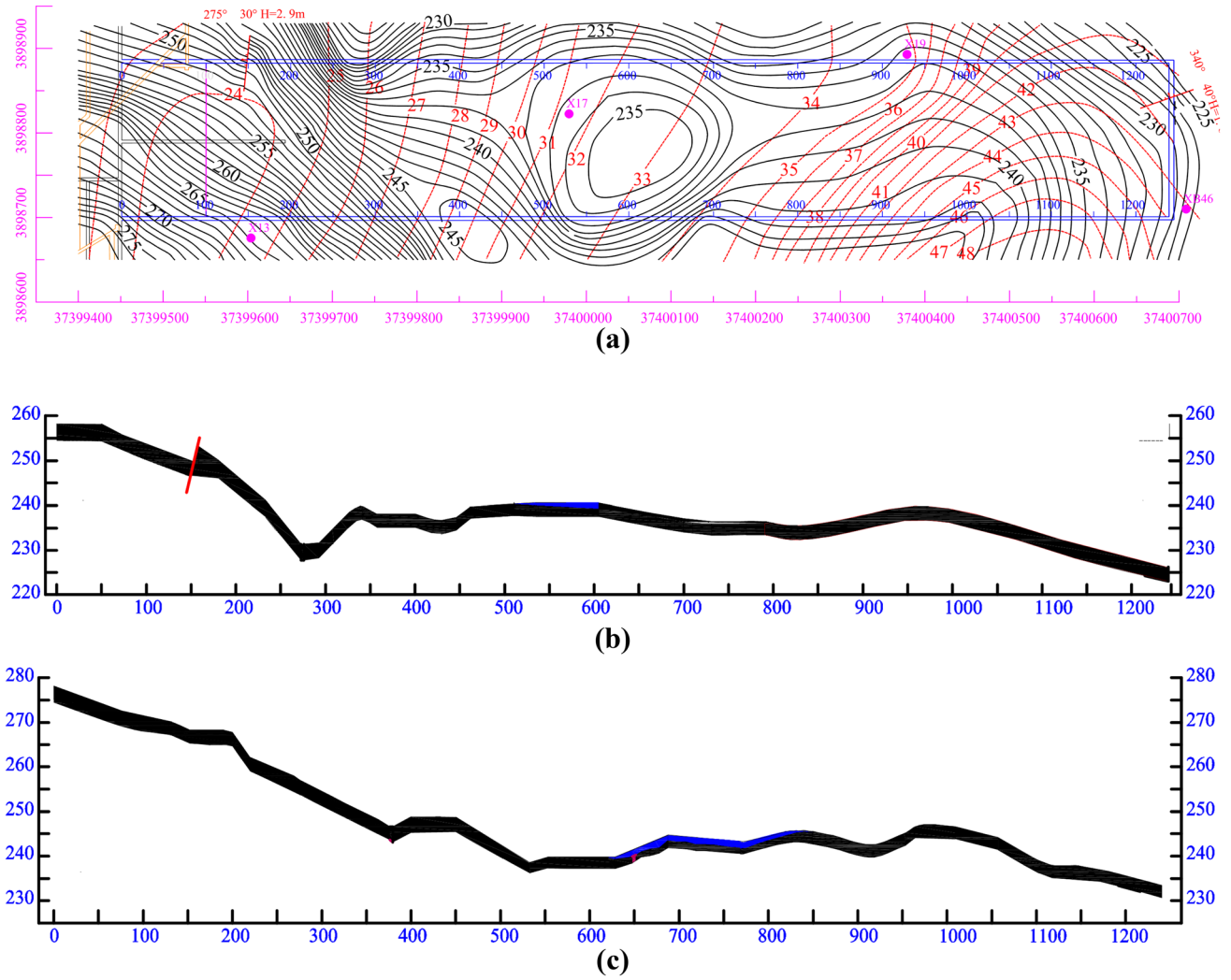

Fig. 3 Geological information for the no. 22517 panel. **a** Contour line of coal seam floor in the No. 22517 Panel (The roadway in the north side was the haulage roadway, the roadway in the south side was the orbital roadway and the roadway in east side was the open-cut. X13, X17 and X19 were boreholes located within the No. 22517 Panel. The pink numbers were longitude and latitude. The blue numbers were pitch distance. The red numbers were the floor thickness between Ordovician limestone and the No. 5 coal seam. The black numbers were elevation of coal seam floor. The unit of the numbers was meter). **b** Side view of the haulage roadway (The X-axis was the pitch distance and Y-axis was elevation. The unit of the numbers was meter). **c** Side view of the orbital roadway (The X-axis was the pitch distance and Y-axis was elevation. The unit of the numbers was meter)

seismic potency, apparent stress, seismic moment, apparent volume, energy index (EI), and Gutenberg-Richter *b* value are important parameters for MS monitoring, these six parameters were used in this study. The physical meanings of these six parameters and specific calculations follow.

1. *Seismic potency (m^3).* The seismic potency represents the inelastic volume deformation at the source of a MS event. Seismic potency can be calculated by formula 1. For a planar shear source, the seismic potency can be calculated by formula 2. At the recording site, Mendecki et al. (2010) calculated seismic potency by formula 3.

$$P = \Delta\varepsilon V \tag{1}$$

$$P = \overline{u}A \tag{2}$$

$$P_{P,S} = 4\pi v_{P,S} R \int_0^{t_s} u_{\mathrm{corr}}(t)dt \tag{3}$$

In formula 1, P is the seismic potency, $\Delta\varepsilon$ is the inelastic shear strain change, and V is the source volume. In formula 2, A is the area of the failure plan and $\overline{u}$ is the relative slip distance on both sides of failure surface. In formula 3, $u_{\mathrm{corr}}(t)$ is the displacement pulse of the P-wave or S-wave, which is corrected for the far-field radiation pattern,$v_{\mathrm{P,S}}$ is the velocity of the *P*-wave or *S*-wave, R is the distance

Fig. 4 Borehole lithology histogram of X17 in floor

Stratigraphic age	Serial number	Elevation	Thickness	Lithology
Lower Permian Syetem Shanxi Formation		240.47 m	3.19 m	No. 5 coal
	1	237.28 m	0.35 m	Fine siltstone
	2	236.93 m	0.80 m	Quartz sandstone
Upper Carboniferous System Taiyuan Formation	3	336.13 m	3.23 m	Fine siltstone
	4	232.90 m	0.32 m	No. 6 coal
	5	232.58 m	1.30 m	Fine siltstone
	6	231.28 m	1.80 m	Quartz sandstone
	7	229.48 m	1.79 m	Fine siltstone
	8	227.69 m	0.36 m	No. 7 coal
	9	227.33 m	2.10 m	Fine siltstone
	10	225.23 m	4.80 m	Fine conglomerate
	11	220.43 m	1.60 m	Fine siltstone
	12	218.83 m	1.60 m	Quartz sandstone
	13	217.23 m	1.25 m	Fine siltstone
	14	215.98 m	1.27 m	Quartz sandstone
	15	214.71 m	1.29 m	No. 10 coal
	16	213.42 m	1.59 m	Fine siltstone
	17	211.83 m	4.00 m	Aluminous mudstone
	18	207.83 m	2.50 m	Glutenite
Middle-lower Ordovician System Majiagou Formation	19	205.33 m	4.40 m	Dolomitic limestone
	20	200.93 m	26.90 m	Limestone
	21	174.03 m	4.00 m	Infilling
	22	170.03 m	14.72 m	Limestone

Table 1 Geological parameters in the No. 22517 Panel

No. 22517 Panel	Mining coal seam		Geometrical size				Water-bearing area with the head of Ordovician limestone water + 375 m
	Coal number	Inclination angle	Length		Width	Average thickness	
	5th	3°	1217 m		185 m	3.3 m	
	From southwest to northeast side						
	Floor elevation		Floor thickness		Water pressure (minimum, maximum)		
	+ 275 m	+ 225 m	24 m	48 m	1.0 MPa	1.5 MPa	
Floor geological information	Distance between the 5th Coal Seam floor and Ordovician limestone is 31.95 m						The type of the floor in the 5th Coal Seam is the sandstone type
	Key strength stratum			Key water isolated stratum			
	Fine conglomerate (thickness 4.8 m)			Aluminous mudstone (thickness 4.0 m)			
	at 12.05 m below the coal seam			at 8.6 m below the fine conglomerate			

Table 2 Overview of abnormal areas based on geological conditions

Geological structures	Locations	Method pf exposure	Note
Fault	At the open cut in Fig. 3	Roadway excavation	The strike is 340°, the dip is 40° and the spacing distance is 1.6 m
Fault	At the pitch distance of 190 m in the haulage roadway in Fig. 3	Roadway excavation	The strike is 275°, the dip is 30° and the spacing distance is 2.9 m
Fault	At the pitch distance from 200 to 350 m in Fig. 3	Microseismic monitoring by Cheng al. (2019)	The strike is 357.5° in the haulage roadway and 307.5° in the orbital roadway. The dip is 73° and the spacing distance is 1 m
Anticline	At the pitch distance from 480 mto720m in Fig. 3	Roadway excavation	The maximum height difference between the core of the anticline and its two wings is 4 m
Thin seam zone	At the pitch distance from 500 to 810 m in the haulage roadway and 530–840 m in the orbital roadway in Fig. 3	Roadway excavation	The thickness of the coal seam decreases from 3.7 to 1.5 m

Table 3 Geophysical prospecting results in the No. 22517 Panel

Zone name	Zone shape	Zone location		Geophysical prospecting method
		In the orbital roadway	In the haulage roadway	
The 1st low resistivity zone	Rectangular area	250–330 m in Fig. 5 a		Direct current method
The 2nd low resistivity zone	Parallelogram area	350–540 m in Fig. 3	490–600 m in Fig. 3	Direct current method
The 3rd low resistivity zone	Parallelogram area	690–980 m in Fig. 3a	690–1050 m in Fig. 3	Direct current method
The anomaly zone	Parallelogram area	220–280 m in Fig. 3	380–530 m in Fig. 3	Transient electromagnetic method

between a sensor and the source, and t_s is the source duration, $u_{\mathrm{corr}}(0) = 0$ and $u_{\mathrm{corr}}(t_s) = 0$.

2. *Seismic* moment (N·M). The seismic moment is used to measure the inelastic deformation at the source, and can be calculated as formula 4. For a planar shear source, the seismic moment can be calculated as formula 5. Based on this, Hanks and Kanamori (1979) defined the moment magnitude to measure the magnitude of a seismic event and established the relationship that scales seismic moment into the moment magnitude as formula 6.

$$M = \mu P \tag{4}$$

$$M = \mu \bar{u} A \tag{5}$$

$$m = \frac{2}{3}\log M - 6.0 \tag{6}$$

Table 4 Coordinates of geophones in the No. 22517 Panel (Cheng et al. 2019)

Number	Location	North (m)	East (m)	Depth (m)	Number	Location	North (m)	East (Y, m)	Depth (m)
1	Orbital roadway	3898695.4	37399555.3	263.1	16	Haulage roadway	3898877.2	37399550.0	246.3
2	Orbital roadway	3898695.6	37399656.9	256.0	17	Haulage roadway	3898888.0	37399641.3	240.0
3	Orbital roadway	3898695.1	37399714.2	251.0	18	Haulage roadway	3898888.0	37399683.2	232.5
4	Orbital roadway	3898694.3	37399781.5	243.5	19	Haulage roadway	3898887.2	37399751.3	225.6
5	Orbital roadway	3898694.3	37399833.7	241.2	20	Haulage roadway	3898887.6	37399811.9	230.3
6	Orbital roadway	3898695.1	37399902.2	240.1	21	Haulage roadway	3898887.8	37399865.8	230.2
7	Orbital roadway	3898695.1	37399971.0	234.1	22	Haulage roadway	3898887.6	37399927.6	232.0
8	Orbital roadway	3898695.4	37400041.0	232.7	23	Haulage roadway	3898888.0	37399985.3	233.4
9	Orbital roadway	3898695.4	37400112.2	235.9	24	Haulage roadway	3898887.3	37400061.3	233.9
10	Orbital roadway	3898695.4	37400176.2	238.4	25	Haulage roadway	3898887.3	37400136.3	231.6
11	Orbital roadway	3898695.4	37400247.1	237.5	26	Haulage roadway	3898887.6	37400203.8	230.1
12	Orbital roadway	3898695.4	37400324.4	237.6	27	Haulage roadway	3898887.6	37400290.8	230.9
13	Orbital roadway	3898695.4	37400414.0	238.1	28	Haulage roadway	3898887.6	37400376.8	233.1
14	Orbital roadway	3898695.4	37400512.0	236.8	29	Haulage roadway	3898887.3	37400448.9	231.9
15	Orbital roadway	3898695.4	37400606.9	230.4	30	Haulage roadway	3898887.5	37400537.4	227.7

Table 5 Parameters of three MS events-concentrated zones

MS events-concentrated zones	Spatial distribution range (pitch distance, m)	Extended depth in floor (m)	Energy density (J/m^3)	Remarks
I	500–630 m	50 m	Largest	Controlled by a fold
II	420–480 m	20 m	Large	Area with high water content
III	330–410 m	30 m	Small	Controlled by a fault revealed by Cheng al. (2019)

Table 6 Content analysis result of the water inflow in the No. 22517 Panel

Test item		Concentration (unit: mg/L)	Molarity (unit: mmol/L)	Mole percent (unit: %)
BC	K^+	4.7	0.1	0.40
	Na^+	219.7	9.6	38.55
	Ca^{2+}	251.8	12.6	50.60
	Mg^{2+}	28.9	2.4	9.64
	$Na^+ NH_4^+$	3.46	0.2	0.80
	$Na^+ \sum$BC	508.56	24.9	100.00
BA	Cl^-	125.7	3.5	21.21
	SO_4^{2-}	282.3	5.9	35.76
	HCO_3^-	425.4	7	42.42
	NO_2^-	5.7	0.1	0.61
	$\sum$BA	839.1	16.5	100.00
pH		7.4		
Salinity		1347.6 mg/L		

where M is the seismic moment, P is the seismic potency, μ is the shear modulus (35.2 GPa), A is the area of the failure plan, $\overline{u}$ is the relative slip distance on both sides of the failure surface, m is the moment magnitude, and M is the seismic moment.

3. *Seismic energy (J)*. The seismic energy, which is radiated as seismic waves, is the portion of the energy that is released during fracture and frictional sliding at the source. Mendecki et al. (2010) calculated the seismic energy of the P-wave or S-wave according to formula 7.

$$E_{P,S} = \frac{8}{5}\pi\rho v_{P,S} R^2 \int_0^{t_s} \dot{u}^2_{\text{corr}}(t)dt \tag{7}$$

where E is the seismic energy, ρ is the rock density, $\dot{u}^2_{\text{corr}}(t)$ is the square of the displacement pulse of the P-wave or S-wave, t_s is the source duration, $v_{P,S}$ is the velocity of the S-wave or P-wave, and R is the distance from the source.

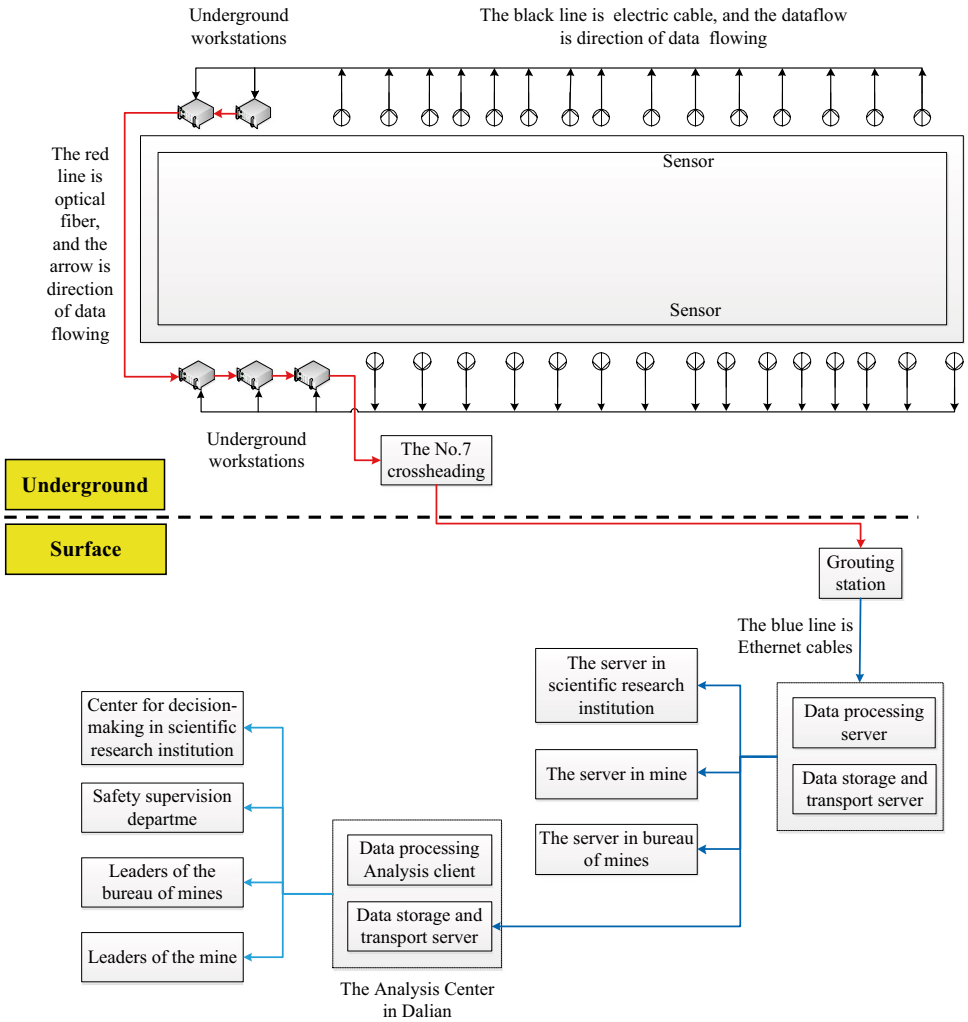

Fig. 5 Data transmission network of MS monitoring system in the no. 22517 panel (Cheng et al. 2017)

4. *Apparent stress (Pa)*. Aki (2012) and Wyss and Brune (1968) calculated the apparent stress as the seismic energy caused by inelastic deformation per unit volume at the source using formula 8.

$$\sigma_A = \frac{E}{P} \tag{8}$$

where σ_A is the apparent stress, E is the seismic energy, and P is the seismic potency.

5. *Energy index*. The average energy corresponding to seismic potency can be calculated by formula 9 from the seismic potency and the seismic energy, calculated as shown in Fig. 1. The energy index was defined by Van and Butler (1993) as the ratio of the seismic energy to the average energy, and was calculated by formula 10.

$$\log\overline{E}(P) = d\log P + c \tag{9}$$

$$EI = \frac{E}{\overline{E}(P)} = \frac{E}{10^{d\log P + c}} = 10^{-c}\frac{E}{P^d} \tag{10}$$

where $\overline{E}(P)$ is the average energy corresponding to seismic potency, P is the seismic potency, E is the seismic energy, EI is the energy index, and c and d are constants.

6. *Apparent volume (m^3)*. The apparent volume was calculated by Mendecki et al. (1993) as formula 11.

$$V_A = \frac{\mu P^2}{E} = \frac{MP}{E} \tag{11}$$

where V_A is the apparent volume, μ is the shear modulus (35.2 GPa), E is the seismic energy, P is the seismic potency, and M is the seismic moment.

7. *Gutenberg-Richter b value*. The seismic size distribution typically follows a power law by Gutenberg and Richter (1944), which can be determined by formula 12. The Gutenberg-Richter b value is the slope of this power law, and is commonly used to describe the relative proportion

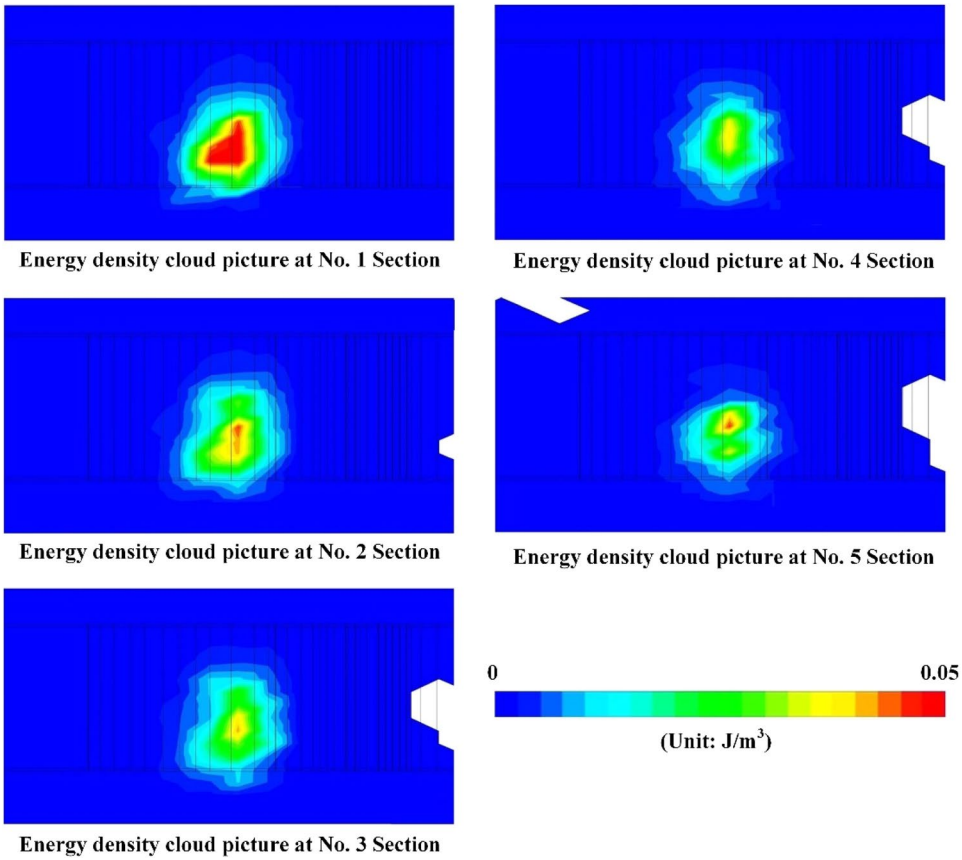

Fig. 6 Change characteristics of the energy density of MS events at different elevation in the MS events-concentrated zone I. (Note: The No. 1 Section is at the elevation of +240 m. The No. 2 Section is at the elevation of +230 m. The No. 3 Section is at the elevation of +220 m. The No. 4 Section is at the elevation of +210 m. The No. 5 Section is at the elevation of +200 m)

of small magnitude events vs. large magnitude events. A large Gutenberg-Richter b value indicates a large proportion of small seismic events. The Gutenberg-Richter b value can be calculated by fitting the seismic size distribution according to formula 12.

$$\log N = a - bm \tag{12}$$

where m is the magnitude of MS events, N is the number of MS events, whose magnitude is not less than m, b is the slope of the power law, and a is a constant representing the seismic activity.

Micro-fracture Precursors of Water-Flow Channels in a Coal Mining Case

The no. 22517 panel in the Dongjiahe coal mine was studied using a MS monitoring system to monitor the evolution characteristics of floor MS events during mining. The Dongjiahe coal mine is located in Shaanxi Province in China (Fig. 2a). The no. 22517 panel is the panel that was being mined during MS monitoring; the lithology of the overlying and floor strata of the panel is shown in Fig. 2b. The formation process of water-flow channels was determined by analysis of hydrological and geological conditions, the change characteristics of water inflow, the water quality of the water inflow, and MS monitoring results. The change characteristics of the six MS parameters were studied during channel formation for the micro-fracture precursors of the water flow channels.

Hydrological and Engineering Geological Conditions

Coal mines are mainly threatened by Ordovician limestone water in the Hancheng, Chenghe, Pubai, and Fugu mining areas in Shaanxi Province. The no. 22517 panel in the Dongjiahe coal mine in the Chenghe mining area was selected to study the micro-fracture precursor of water-flow

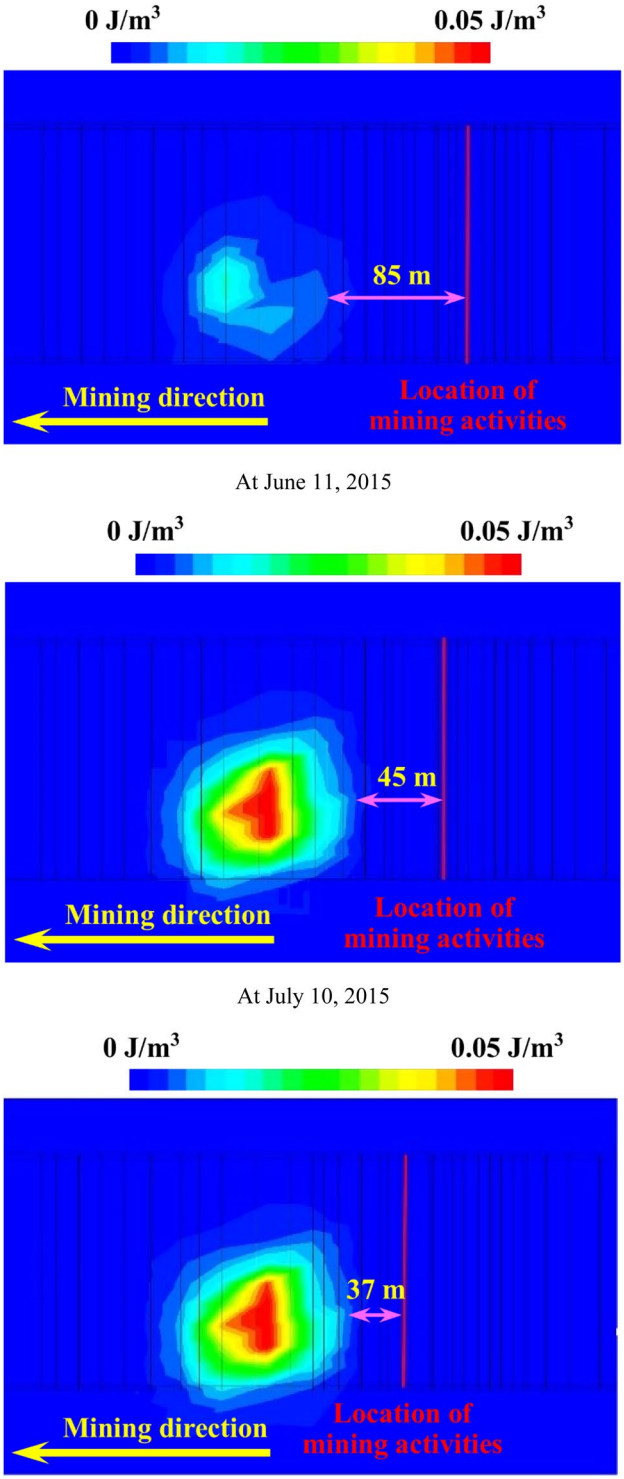

Fig. 7 Formation of the MS events-concentrated zone I

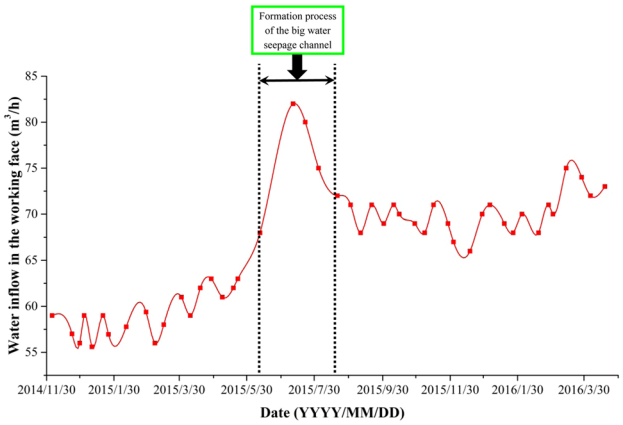

Fig. 8 Change characteristics of water inflow in the no. 22517 panel during the mining process

channels induced by mining. The detailed information and the rock mass strata at this site were described previously (Cheng et al. 2017) and the geological parameters are listed in Table 1.

This study focused on the hydrological and engineering geological conditions at this site (Fig. 3). The blue number in Fig. 3a indicates the pitch distance, which is defined as the distance from a location in the no. 22517 panel to the north–south roadway at the western side of that panel. As shown in Fig. 3, the pitch distance was defined as the horizontal distance from a point in the working face to the north–south roadway at the western side of the working face and was used to describe both the advancing position of mining activities and the spatial location of geological structures. The open cut is located at the eastern side of the no. 22517 panel at a pitch distance of 1217 m, and the mining stop line is located at the western side of that panel, with a pitch distance of 100 m. The north side is the haulage roadway and the south side is the orbital roadway. As shown in Fig. 3, two faults, an anticline, and a thin seam zone were exposed during the excavation of the haulage roadway and the orbital roadway and a fault was exposed by microseismic monitoring during mining of the no. 22517 panel (Cheng al. 2019). The location and parameters of the faults, anticline, and thin seam zone are shown in the Table 2. As shown in Fig. 4, the distance between the floor of the no. 5 coal and the top of the Ordovician limestone was about 31.95 m. A layer of fine conglomerate (4.8 m thick) 12.05 m below the coal seam (Fig. 4) was the stratum with the greatest strength and thickness between the floor of the no. 5 coal and the top of the Ordovician limestone, and so acted as a key strength

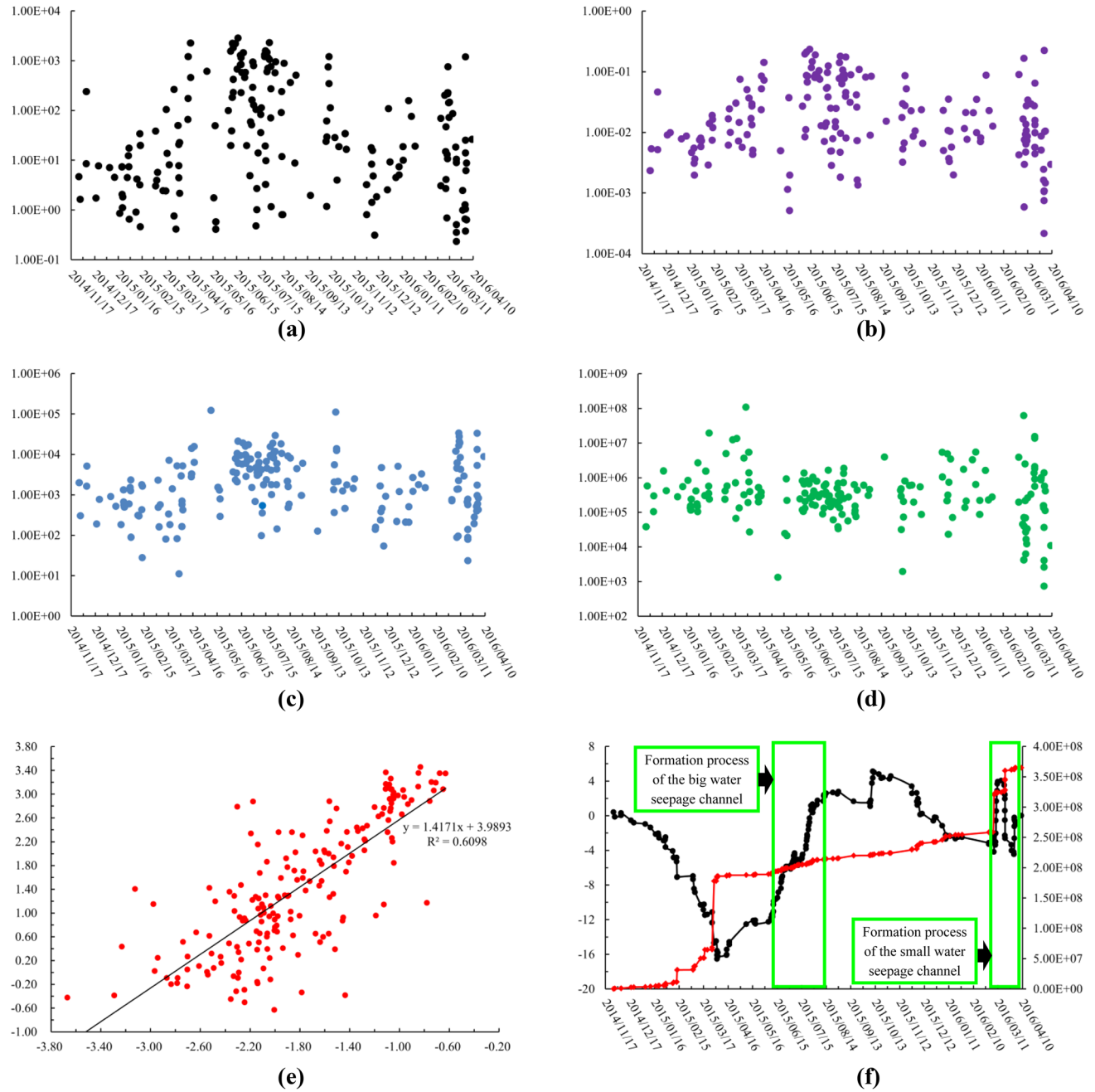

Fig. 9 Change of focal parameters during formation of water flow channels. **a** Evolution characteristics of seismic energy with time during mining process (Y-axis is seismic energy and the unit is J. X-axis is the date). **b** Evolution characteristics of seismic potency with time during mining process (Y-axis is seismic potency and the unit is m3. X-axis is the date). **c** Evolution characteristics of apparent stress with time during mining process (Y-axis is apparent stress and the unit is Pa. X-axis is the date). **d** Evolution characteristics of apparent volume with time during mining process (Y-axis is apparent volume and the unit is m3. X-axis is the date). **e** Fitting formula between the logarithm of seismic potency and the logarithm of seismic energy can be fitted (Y-axis is the logarithm of seismic energy. X-axis is the logarithm of seismic potency). **f** Evolution characteristics of cumulative *EI* (red line) and cumulative apparent volume (black line) with time during mining process (Y-axis in the left is cumulative *EI*. Y-axis in the right is cumulative apparent volume. X-axis is the logarithm of seismic potency)

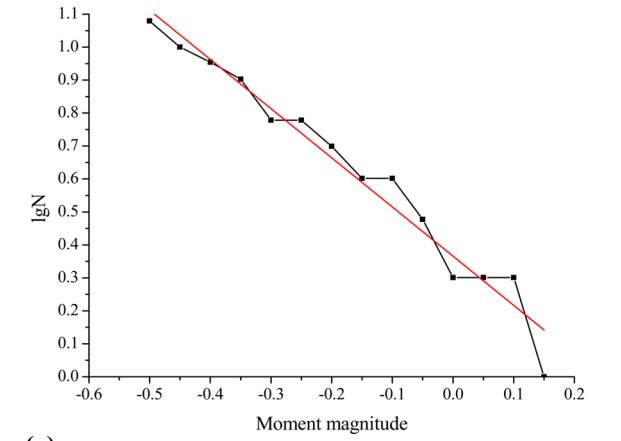

(a) Calculation of the Gutenberg-Richter b value in March 2015

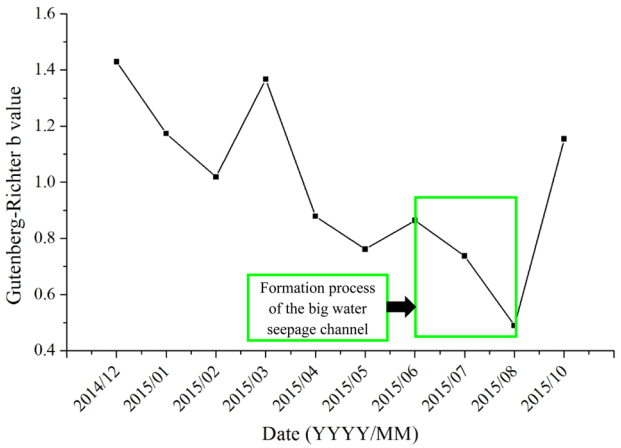

(b) Change characteristics of Gutenberg-Richter b value with time

Fig. 10 Evolution of Gutenberg-Richter b value with time

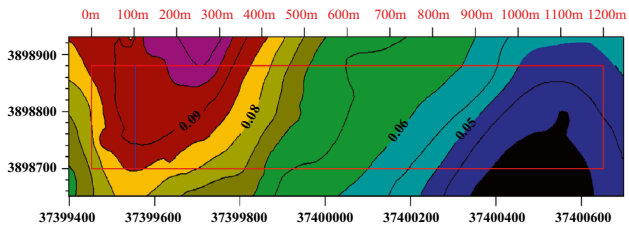

Fig. 11 Distribution of floor water inrush coefficient in the no. 22517 panel

stratum. A layer of aluminous mudstone (4 m thick), 8.6 m below the fine conglomerate (Fig. 4) had strong water resistance performance and acted as a key water-isolating stratum. Meng et al. (2012) divided the coal seam floor lithology into mudstone, mudstone-sandstone, and sandstone based on the mudstone content. As shown in Fig. 4, the mudstone content of the study region is 12.52%. The floor in the no. 22517 panel was the sandstone type, and the floor has high strength and permeability.

Because the no. 5 coal was close to the Ordovician limestone, grouting reinforcement was conducted in the panel's floor strata. The grouting boreholes were positioned at depths from 20.7 to 29.2 m, with an average depth of 25.6 m. After the grouting reinforcement, the transient electromagnetic (TEM) and direct current (DC) measurement methods were used to detect water-rich areas in the no. 22517 panel. Three low resistivity zones and four high resistivity zones were revealed by the DC method and an anomaly zone was revealed by the TEM method. The location and shape of the three low resistivity zones and the anomaly zone are shown in Table 3.

MS Monitoring System

The MS monitoring system in this location was previously described by Cheng et al. (2017). Geophones with a sensitivity of 43.3 V/m/s, and a response frequency from 15 to 1000 Hz were arranged at the non-mining wall of the roadway and in the no. 22517 panel. Fifteen geophones were positioned in the haulage roadway and 15 geophones were positioned in the orbital roadway; the location coordinates are listed in Table 4. To firmly attach the geophones to the rock wall, a borehole length of ≈ 4 m was used to install the geophones perpendicular to the roadway direction, angled downward at 45°.

The geophones were positioned ≈ 80 m apart on each roadway. The data transmission network of the MS monitoring system is shown in Fig. 5. A Geiger localization algorithm (Khadhraoui et al. 2010) method was used to locate the MS events. Use of this algorithm requires detection of the waveform of each MS event by at least four geophones. A homogeneous velocity model was also used to locate MS events. To determine the P- and S-wave velocities, some blasting events with known coordinates were analyzed. The calibration results indicated that the P-wave velocity was 2800 m/s and the S-wave velocity was 1800 m/s. Cheng et al. (2017) calculated the localization error of the MS monitoring system as within 10 m the range of 100 m below the panel's coal seam floor.

Formation of Water Flow Channels

The monitoring results showed that most of the floor MS events were concentrated above the key strength stratum in the no. 22517 panel (12 m below the no. 5 coal), except for three MS events-concentrated zones (zones I, II, and III), which had the potential to form water-flow channels. The parameters and location of these three MS events-concentrated zones are introduced in Table 5. As shown in Table 5, the MS events-concentrated zone I had the largest the extended depth (about 50 m) and energy density. Thus, this zone was most likely to form a water flow channel.

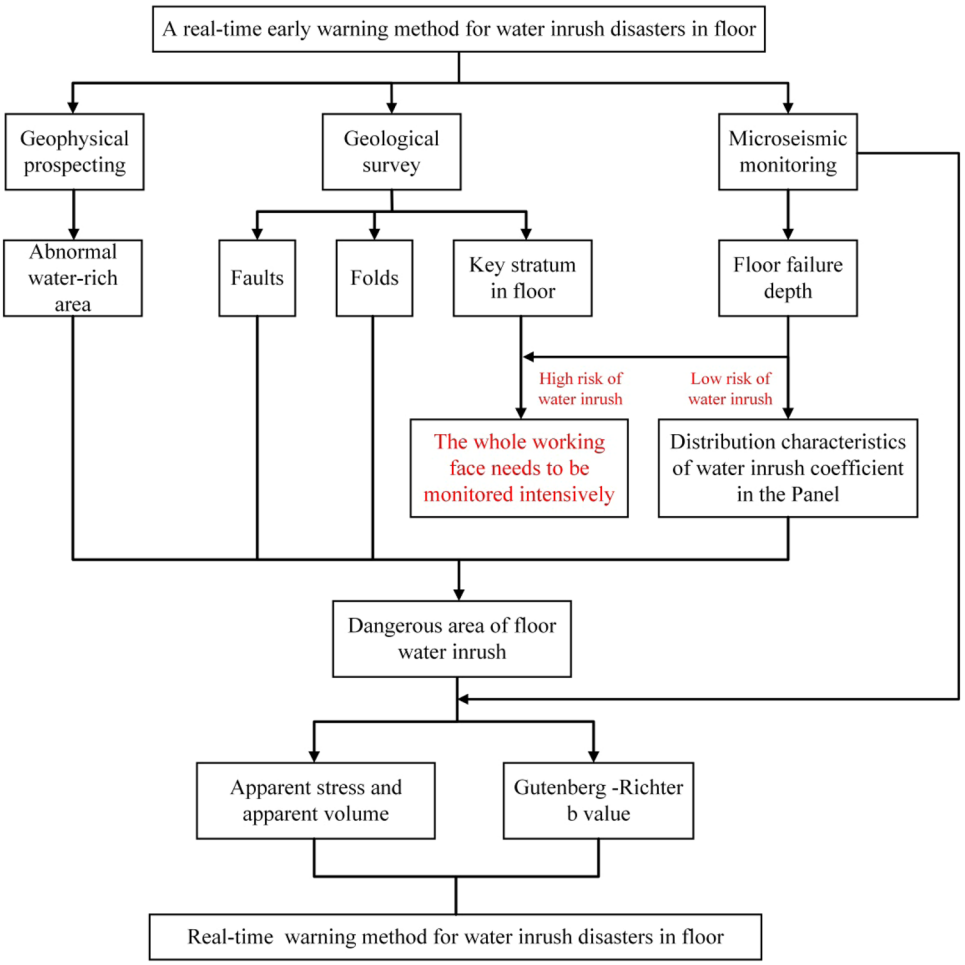

Fig. 12 A real-time early warning method for water inrush disasters in floor

Formation of a water flow channel requires that the local failure area in the floor penetrates the rock mass between the Ordovician limestone roof and the coal seam floor, significantly increasing the water inflow in the panel during formation of the local failure area. Based on geological conditions in the no. 22517 panel, the elevation varied from + 230 m to + 240 m and the elevation in the Ordovician limestone roof varied from + 200 m to + 210 m in the MS events-concentrated zone I. Thus, the change characteristics in energy density of the MS events at different elevation was analyzed from the elevation of + 240 m to the elevation of + 210 and the result was shown in Fig. 6 when the threshold of the energy density of MS events was 0.05 J/m^3. There are four sections in Fig. 6 (the no. 1 section at the elevation of + 240 m, the no. 2 section at the elevation of + 230 m, the no. 3 section at an elevation of + 220 m, and the no. 4 section at an elevation of + 210 m. Of these, the no. 3 section (at + 220 m) was located at the bottom of the key strength stratum. As shown in Fig. 6, the MS events-concentrated zone I gradually decreased at greater depths. The MS events in the MS events-concentrated zone I passed through the key strength stratum and extended to below + 200 m in elevation. Thus, the MS events-concentrated zone I penetrated the rock mass between the Ordovician limestone roof and the coal seam floor.

On this basis, the relationship between the formation process of the MS events-concentrated zone I (Fig. 7) and the change characteristics of water inflow in the no. 22517 panel during the mining process (Fig. 8) was analyzed. As shown in Fig. 7, the number (energy) of the MS events in the MS events-concentrated zone I started to increase on June 11, 2015 (the MS events-concentrated zone I was 85 m from the mining at the time), which meant that the MS events-concentrated zone I began to form. The number (energy) of MS events in the floor peaked on July 10, 2015 (the MS events-concentrated zone I was 45 m from mining activities at that time), which meant that the MS events-concentrated zone I had formed. The number (energy) of MS events in the floor descended to a stable value on July 23, 2015 (the MS events-concentrated zone I was 37 m from mining at that time), which meant that the MS events-concentrated zone I remained unchanged. As shown in Fig. 8, the working face inflow remained unchanged at 60 m^3/h before July 10, 2015. There was a significant increase in water inflow in the

no. 22517 panel from June 11, 2015 to July 10, 2015 and it peaked at 82 m^3/h on July 10, 2015. After July 10, 2015, the working face inflow began to decrease until July 23, 2015. The working face inflow was stable at 70 m^3/h after July 23, 2015. Previous results showed that the formation of the MS events-concentrated zone I corresponded with increasing water inflow in the no. 22517 panel.

The source of the water inflow in the no. 22517 panel is required to further verify the formation of a water channel in this area, so the water flowing into the no. 22517 panel was analyzed (Table 6). There were four hydrochemical types of Ordovician limestone water in the Weibei Mining Area (Tao 1999). The first type was $HCO_3 - Ca$, the second type was $SO_4 \bullet HCO_3 - Na \bullet Ca$, the third type was $SO_4 \bullet HCO_3 - Na \bullet Ca \bullet Mg$ and the forth type was $SO_4 \bullet HCO_3 \bullet Cl - Na \bullet Ca \bullet Mg$. The salinity of the Ordovician limestone water in the Weibei mining area was about 1 g/L. Because the Dongjiahe coal mine was located in the Weibei mining area, it could be inferred that the hydro-chemical type of the water inflow was $SO_4 \bullet HCO_3 \bullet Cl - Na \bullet Ca \bullet Mg$ and most of the water inflow came from the Ordovician limestone water in the no. 22517 panel.

As previously discussed, zone I penetrated the rock mass between the Ordovician limestone roof and the coal seam floor, which meant that zone I had the necessary conditions to form a water flow channel. Indeed, since the formation of zone I corresponded with the increase in water inflow and most of the water came from the Ordovician limestone, it is clear that Ordovician limestone water entered the no. 22517 panel through a water flow channel formed in zone I and the threshold of the energy density of MS events in the in the no. 22517 panel was 0.05 J/m^3. The same method was used to analyze the MS events-concentrated zone III and revealed that a small water flow channel also formed there.

Micro-fracture Precursors of Water Flow Channels

The focal parameters were calculated to characterize their evolution over time as the no. 22517 panel was mined (Fig. 9). The cumulative apparent volume increased significantly as the large and small water flow channels formed. With a month as the time window, the power law was used to fit the moment magnitude distribution of floor MS events, and the Gutenberg-Richter b value of each month was calculated (Fig. 10a) and the change of Gutenberg-Richter *b* value with time was obtained (as shown in Fig. 10b). From Fig. 10b, it can be seen that the Gutenberg-Richter *b* value generally showed a downward trend before the formation of the big water-flow channel, dropped to 0.7 at the start of channel formation, dropped to the lowest value of 0.5 during channel formation, and then increased. The calculations indicate that the cumulative apparent volume increased significantly and the rapid decrease of the Gutenberg-Richter *b* value can be regarded as the micro-fracture precursor of the formation of a water-flow channel, with a value of 0.7 as an early warning threshold for channel formation.

Discussion

Feasibility Analysis on Early Warning for Floor Water Inrush Disasters

Meng et al. (2012) improved the empirical formula (Zhang 2016) to calculate the water inrush coefficient by considering the height of the zone of water rising from the confined aquifer and the floor failure depth, presented as formula 13. In China's Regulations on Water Prevention and Control in Coal Mines, the threshold of water inrush coefficient is set as 0.06 MPa/m in regions with geological structures (such as areas of abnormal water richness, fault areas, and fold areas) and 0.1 MPa/m in other regions.

$$T_S = \frac{P}{M - C_P - Z_0} \tag{13}$$

where T is the coefficient of water inrush, with units of MPa/m, P is the water pressure caused by the confined aquifer in floor, M is the thickness of the floor aquifer, with units of m, C_p is the floor failure depth, with units of m, and Z_0 is the height of the zone of water rising from the confined aquifer.

Calculation of the water inrush coefficient in the no. 22517 panel required determination of the depth of the floor failure and the height of the zone of water rising from the confined aquifer. Gu et al. (2011) used elastic wave velocity monitoring in a borehole to monitor floor failure depth at this location and reported a floor failure depth of 12 m. Because aluminous mudstone has good water-resisting property, the height of the zone of water rising from the confined aquifer is 0 m. The water inrush coefficient at different locations of the no. 22517 panel was calculated using formula 2, allowing construction of a contour map of the water inrush coefficient, presented in Fig. 11. As shown in Fig. 11, the water inrush coefficient was large (0.95 MPa/m) at the northwest end and small (0.04 MPa/m) at the southeast end. In the inverted trapezoidal area from the pitch distance of 0 m to that of 900 m at the haulage roadway and the pitch distance of 0 m to that of 600 m at the orbital roadway of the no. 22517 panel, the water inrush coefficient in floor was greater than 0.06 MPa/m.

The region from 190 m to that of 720 m (the pitch distance) in the no. 22517 panel includes many geological structures (as shown in Table 2) and four water-rich abnormal areas (Table 3). According to Tables 5 and 3, the location of the MS events-concentrated zone I, where a big water-flow channel formed, corresponded with the location of the 2nd low resistivity zone. The location of the MS events-concentrated zone III, where a small water-flow channel formed, corresponded with the location of the 1st low resistivity zone and the anomaly zone. It could be seen that water flow channels are often generated in areas where water-rich geophysically abnormal areas and abnormal areas determined by the water inrush coefficient overlap, but not all overlapping areas form water flow channels. However, our work has shown that the formation of water flow channels can be quantitatively analyzed by using MS monitoring to determine the micro-fracture precursors of water-flow channels.

A Real-Time Early Warning Method

Based on the above results, a real-time early warning method for water inrush disasters in the floor was established (Fig. 12). This method has three steps. In the first step, the overall risk assessment of water inrush disasters in the floor from a panel is evaluated. If the risk of water inrush is high, the panel should not be mined until it meets safe mining standards by grouting reinforcement of the floor strata. If the risk of water inrush disasters is low and the overall stability of the panel is good, local dangerous areas in the floor are identified (the second step). In the third step, MS monitoring is installed in the panel and the localized, potentially dangerous areas are monitored in real time for early detection of water inrush disasters.

In the first step, hydrologic and engineering geological information is acquired by geological survey and geophysical prospecting. Geological information (coal seam thickness, floor lithology distribution, and thickness, water-proof layer distribution and spatial thickness, key stratum spatial location and thickness, Ordovician limestone aquifer spatial location, and water pressure distribution) is acquired using geological exposures, such as boreholes, roadway excavation, and mining activities. Geophysical prospecting is performed using seismic wave, ground penetrating radar, audio-frequency electrical penetration, transient electromagnetics, and high-density resistivity methods. Geophysical prospecting provides the spatial location of failure zones, faults, folds, and collapse columns, as well as the water content of these features. Next, the floor failure depth should be determined and the overall risk assessment of water inrush disasters through the floor from the work surface can be evaluated by assessing the potential correlation between the spatial location of the key stratum and the floor failure zone. If the floor failure zone in a panel passes through the key stratum in floor, then grouting of this stratum is needed to reduce the failure depth. However, the floor in the no. 22517 panel was found to be stable.

In the second step, the water inrush coefficient is calculated by formula 2 based on the height of the zone of water rising from the confined aquifer and the floor failure depth. The coefficient data is then presented as a contour map of the area of interest. Using the water inrush coefficient thresholds stipulated by the Regulations on Water Prevention and Control in Coal Mines for normal regions and regions with geological structures, potentially dangerous areas can be identified.

In the third step, a MS monitoring system is established to monitor in real time the evolution characteristics of floor MS events in areas with a risk of a water inrush disaster. These collected data allow calculation of the cumulative apparent volumes and the Gutenberg-Richter b values. In this way, monitoring is performed in real time for the early detection of water inrush disasters induced by mining activity in coal mines.

Conclusion

1. Using MS monitoring technology to monitor the formation process of water flowing channels was shown to be feasible. The energy density of MS events were used to comprehensively determine the energy aggregation and quantity aggregation of MS events to identify the spatial location and formation of water flow channels. This information, along with the MS focal parameters of seismic energy, seismic potency, apparent stress, seismic moment, apparent volume, energy index (EI) and Gutenberg-Richter b value were used in this study to detect micro-fracture precursors of water-flow channels induced by mining activity.
2. In the no. 22517 panel in the Dongjiahe coal mine, the formation of water-flow channels was described by analysis of the hydrological and geological conditions, changes in water inflow during the mining process, the water quality of the water inflow, and MS monitoring results. The detected MS data was temporally and spatially consistent with formation of a water channel, and was used to identify the spatial location and formation of the water flow channels in the no. 22517 panel, where the threshold of the energy density of MS events was 0.05 J/m^3, which can provide reference for mines with similar engineering geological conditions. The change characteristics of MS focal parameters were studied during channel formation, and the significant increase in cumulative apparent volume and rapid decrease of

the Gutenberg-Richter b value correspond to the microfracture precursor of channel formation. The data suggest that a Gutenberg-Richter b value of 0.7 should be an early warning threshold for channel formation.

3. The feasibility for a real-time early warning for water inrush disasters through the coal seam floor was studied based on previous research results and after determining it was feasible to establish a real-time early warning method using MS monitoring, geophysical prospecting, and water inrush coefficients, a real-time early warning method for water inrush disasters through floor was established using these methods.

Acknowledgements This work was funded by the National Science Foundation of China (Grants 51909032 and U1710253, 51627804, 51879041), Natural Science Foundation of Anhui Province (Grant 2008085ME145) and Fundamental Research Funds for the Central Universities (Grant N180105029).

Data Availability Some or all data, models, or code generated or used during the study are available from the corresponding author by request.

References

Aki K, Richards PG (2012) Quantitative seismology. University Science Books, California

Chen B, Feng X, Zeng X, Xiao Y, Zhang Z, Ming H, Feng G (2011) Real-time microseismic monitoring and its characteristic analysis during TBM tunneling in deep-buried tunnel. Chin J Rock Mech Eng 30(2):275–283 (**in Chinese**)

Chen L, Liu J, Wang C, Wang L, Wang X, Wang J (2012) Study of acoustic emission characteristics of Beishan deep granite under different stress conditions. Chin J Rock Mech Eng 31:3618–3624 (**in Chinese**)

Cheng G, Ma T, Tang C, Liu H, Wang S (2017) A zoning model for coal mining-induced strata movement based on microseismic monitoring. Int J Rock Mech Min 94:123–138

Cheng G, Li L, Zhu W, Yang T, Tang C, Zheng Y, Wang Y (2019) Microseismic investigation of mining-induced brittle fault activation in a Chinese coal mine. Int J Rock Mech Min 123:104096

Du W, Jiang Y, Ma Z, Jiao Z (2017) Assessment of water inrush and factor sensitivity analysis in an amalgamated coal mine in China. Arab J Geosci 10(21):471

Fan K, Li W, Wang Q, Liu SL, Xue S, Xie C, Wang Z (2019) Formation mechanism and prediction method of water inrush disasters from separated layers within coal seam mining: a case study in the Shilawusu mining area, China. Eng Fail Anal 103:158–172

Gu S, Li A, Su P (2011) The report on the distribution characteristics of the floor failure depth and waterproof measures in the Chenghe mining area. Xi'An University of Science and Technology, Xi'An

Gutenberg B, Richter CF (1944) Frequency of earthquakes in California. B Seismol Soc Am 34(4):185–188

Hanks TC, Kanamori H (1979) A moment magnitude scale. J Geophys Res 84(B5):2348–2350

Hua X, Zhang W, Jiao D (2011) Assessment method of water-inrush risk induced by fault activation and its application research. Proced Eng 26:441–448

Khadhraoui B, Leslie D, Drew J (2010) Real-time detection and localization of microseismic events. SEG Technical Program Expanded Abstracts, Soc of Exploration Geophysicists, pp 2146–2150

Lei X, Kusunose K, Satoh T, Nishizawa O (2003) The hierarchical rupture process of a fault: an experimental study. Phys Earth Planet Inter 137(1–4):213–228

Li T, Liu J, Chen L, Xu J, Wang L (2013) Acoustic emission characteristics of granite under tensile loading. Chin J Rock Mech Eng S2:3215–3221

Li L, Zhou Z, Li S, Xue Y, Xu Z, Shi S (2015) An attribute synthetic evaluation system for risk assessment of floor water inrush in coal mines. Mine Water Environ 34(3):288–294

Li S, Wu J, Xu Z, Yang W (2019) Mechanics criterion of water inrush disasters from the coal floor under influence of fault and its engineering application. Int J Geomech 19(5):04019022

Liu J, Feng X, Li Y, Xu S, Sheng Y (2013) Studies on temporal and spatial variation of microseismic activities in a deep metal mine. Int J Rock Mech Min 60:171–179

Liu C, Wu S, Cheng A (2014) Microseismic monitoring and numerical simulation of the formation of water inrush disasters pathway caused by coal mining. J Univ Sci Technol Beijing 09:1129–1135 (**in Chinese**)

Lynch R, Mendecki A (2004) Experimental and theoretical investigations of fundamental processes in mining induced fracturingand rock instability close to excavations. ISS International Limited, Abu Dhabi

Mendecki A, Keynote A (1993) Real time quantitative seismology in mines. Proc, 3rd international symp on rockbursts and seismicity in mines, pp 287–295

Mendecki A, Lynch R, Malovichko D (2010) Routine micro-seismic monitoring in mines. Proc, Australian earthquake engineering soc conf, pp 1–33

Meng Z, Li G, Xie X (2012) A geological assessment method of floor water inrush disasters risk and its application. Eng Geol 143:51–60

Qiao W, Li W, Zhao C (2009) Water inrush coefficient-unit inflow method for water inrush disasters evaluation of coal mine floor. Chin J Rock Mech Eng 28(12):2466–2474 (**in Chinese**)

Tao S (1999) The chemical characteristics and geological background of karst water in north Weinan, Shaanxi. Geol Shaanxi 01:53–57 (**in Chinese**)

Van Aswegen G, Butler AG (1993) Applications of quantitative seismology in South African gold mines. In: Young RP (Ed), Proc, 3rd symp on rockbursts and seismicity in mines, pp 261–266

Wu Q, Liu Y, Luo LH, Liu S, Sun W, Zeng Y (2015) Quantitative evaluation and prediction of water inrush vulnerability from aquifers overlying coal seams in Donghuantuo coal mine, China. Environ Earth Sci 74(2):1429–1437

Wu J, Xu S, Zhou R, Qin Y (2016) Scenario analysis of mine water inrush disasters hazard using Bayesian networks. Saf Sci 89:231–239

Wu Q, Zhao D, Wang Y, Shen J, Mu W, Liu H (2017) Method for assessing coal-floor water-inrush risk based on the variable-weight model and unascertained measure theory. Hydrogeol J 25(7):2089–2103

Wyss M, Brune JN (1968) Seismic moment, stress, and source dimensions for earthquakes in the California-Nevada region. J Geophys Res 73(14):4681–4694

Xiao Y, Feng X, Hudson JA, Chen B, Feng G, Liu J (2016) ISRM suggested method for in situ microseismic monitoring of the fracturing process in rock masses. Rock Mech Rock Eng 49(1):343–369

Xie H, Liu J, Ju Y, Li J, Xie L (2011) Fractal property of spatial distribution of acoustic emissions during the failure process of bedded rock salt. Int J Rock Mech Min 48(8):1344–1351

Xu Z, Wu J, Li S, Zhang B (2017) Semianalytical solution to determine minimum safety thickness of rock resisting water inrush disasters from filling-type karst caves. Int J Geomech 18(2):04017152

Yang B, Sui W, Duan L (2017) Risk assessment of water inrush disasters in an underground coal mine based on GIS and fuzzy set theory. Mine Water Environ 36(4):617–627

Yu Q, Tang C, Li L, Cheng G, Tang L (2015) Study on rockburst nucleation process of deep-buried tunnels based on microseismic monitoring. Shock Vib 1:685437

Zhang F (2016) Study on deformation failure mechanism of deep coal seam floor and evaluation method of water inrush disasters mining above confined aquifer. PhD Diss, China Univ of Mining and Technology (in Chinese)

Zhang P, Yang T, Yu Q, Xu T, Shi W, Li S (2016) Study of a seepage channel formation using the combination of microseismic monitoring technique and numerical method in Zhangmatun iron mine. Rock Mech Rock Eng 49:3699–3708

Zhao D, Wu Q, Cui F, Xu H, Zeng Y, Cao Y, Du Y (2018) Using random forest for the risk assessment of coal-floor water inrush disasters in Panjiayao coal mine, northern China. Hydrogeol J 26(7):1–14

Zhou J, Yang T, Zhang P, Xu T, Wei J (2017) Formation process and mechanism of seepage channels around grout curtain from microseismic monitoring: a case study of Zhangmatun iron mine, China. Eng Geo 226:301–315